Surfaces and Interfaces xxx (xxxx) 109054

Contents lists available at ScienceDirect

Surfaces and Interfaces

journal homepage: www.elsevier.com/locate/surfin

Effects of simulated lung fluid (SLF) on fibrous zeolites through real-time SC-XRD investigations

Matteo Giordani [a,*], Michele Mattioli [a], Georgia Cametti [b]

[a] Department of Pure and Applied Sciences, University of Urbino Carlo Bo, Urbino 61029, Italy
[b] Institute of Geological Sciences, University of Bern, Baltzerstrasse 1 + 3, Bern 3012, Switzerland

ARTICLE INFO

Keywords:
Erionite
Offretite
Mordenite
SLF interaction
SC-XRD
Carcinogenicity

ABSTRACT

Zeolites are minerals widely distributed in many geological contexts and, due to their unique properties, are currently used in a multitude of processes. Among them, the fibrous zeolite erionite is carcinogenic to humans via inhalation, and its interaction with biological systems has been extensively investigated over the past decades. However, the reasons for its toxicity are still unclear, and other fibrous zeolites are currently being studied by the scientific community. This study investigated the chemical and structural modifications of three natural fibrous zeolites (offretite, mordenite, and erionite) in contact with simulated lung fluid (SLF) as a function of interaction time. The results show that all tested zeolites immersed in SLF behave similarly, exchanging the extra-framework cation Ca^{2+} with the Na^{+} from the solution. Thus, similarly to erionite, mordenite and offretite fibres can also release calcium in the lung environment. The refined chemical composition of offretite pointed to an unbalanced formula, with a significant lack of positive charges due to Ca^{2+}-Na^{+} substitution. Such a lack could be balanced by protons attached to framework oxygen atoms, originating Brønsted acid sites. This finding is of paramount importance since surface protons and OH groups could modify the acidity of the zeolites, potentially increasing their chemical reactivity and, consequently, enhancing the carcinogenic response.

1. Introduction

Minerals of the zeolite group are widely distributed in different geological environments. Owing to their unique properties such as cation exchange, absorbent capability, dehydration, etc., zeolites are currently used in a wide range of applications, including the building industry, gas separation and purification, catalysis and as sorbents for environmental remediation processes [1–2].

The fibrous zeolite erionite is recognized as a human carcinogen [3]. Consequently, there is growing concern regarding the potential health risks associated with environmental and occupational exposure to erionite in several countries, including Turkey, USA, Mexico, Iran, Italy and New Zealand [4–9]. Similarly, other fibrous zeolites (e.g. offretite, mordenite, mesolite and ferrierite) are currently under investigation by the scientific community to assess their potential effects on human health [10–13 and references therein]. Mordenite is widely used in industry (petrochemicals, catalysis, sensors, gas–liquid separation), but its toxicological properties remain poorly studied despite its similarity to the fibrous erionite [14–20]. Existing studies are few and often methodologically weak, leading the IARC to classify mordenite as a Group 3 carcinogen [3]. Offretite, though rarer, is chemically and structurally similar to erionite and warrants further investigation [12]. A fundamental point to prevent future epidemics related to the dispersion of mineral fibres is to understand, in advance, the health effects of inhaling such particulates resulting from weathering, mining activities, industrial and/or agricultural applications. Current knowledge of the biological processes triggered by inhalation of fibrous zeolites remains extremely scarce. The only exception is erionite, which has been extensively studied over the past decades, although many aspects of its pathogenicity are still under debate. The changes/transformations occurring at the lung cell/mineral fibre interface represent a critical stage in potentially triggering the cascade processes that may lead to the development of lung diseases, particularly malignant mesothelioma. Many aspects have key roles in toxic and carcinogen processes of mineral fibres, such as size and fibre morphology, biodurability, chemical composition, the presence of iron and other toxic and radioactive elements, linked impurities and many others [21–27]. One of the most critical aspects that remains poorly understood is the effect of cation-exchange properties of fibrous zeolites on human health. Different studies demonstrated that erionite fibres are generally too short to induce “frustrated

* Corresponding author.
E-mail address: matteo.giordani@uniurb.it (M. Giordani).

https://doi.org/10.1016/j.surfin.2026.109054
Received 19 September 2025; Received in revised form 26 February 2026; Accepted 18 March 2026
2468-0230/© 20XX

UNCORRECTED PROOF

Note: Low-resolution images were used to create this PDF. The original images will be used in the final composition.

phagocytosis" but can alter cellular homeostasis via cation-exchange, triggering biological effects [28]. Erionite is capable of exchanging ions, particularly its most abundant extra-framework (EF) cations (K^+, $Ca2^+$, Na^+, Mg^{2+}), with extracellular and intracellular K^+, Na^+, and Ca^{2+} present in lung lining fluids and in the cytosol [29–30]. In this context, several authors have recently focused on the nature of the exchange processes between simulated pulmonary solutions and erionite fibres. Crystal chemical and structural modifications of erionite-Na leached with simulated lung fluids (SLFs) were firstly investigated by Ballirano and Cametti [31], showing a migration of Na^+ to a different EF cationic site of erionite or a temporary partial replacement of Na^+ by Ca^{2+}, after interaction with artificial lysosomal fluid (ALF) and Gamble's solution, respectively. Giordani and coauthors [32] investigated erionite-Ca and offretite during interactions with ALF (pH ≈ 4) and Gamble's solution (pH ≈ 8), showing the processes affecting the surface of the crystals. Real-time imaging by Atomic Force Microscopy showed particle detachment from the zeolite surfaces, superficial dissolution in ALF, and the formation of a thin layer of a new phase in Gamble's solution. Pacella and coauthors [33] reported the surface and bulk modifications of erionite-K in contact with a mimicked Gamble's solution. Their results demonstrated that erionite is more biodurable than asbestos and can bind Na from the lung fluid within 24 h of incubation. Significant release of K^+, Ca^{2+}, and Mg^{2+} was also observed, but the contribution of accessory minerals like chabazite and nontronite was included. Di Carlo and coauthors [34] incubated mineral fibres first in an extracellular environment and then in an intracellular cytosol medium. Their study showed that erionite primarily uptakes Na^+ from the extracellular fluid and exchanges it with the cytosolic K^+. Moreover, the authors suggested that phagocytized erionite cannot reduce cytosolic Ca^{2+} levels and alter the endoplasmic reticulum-mitochondria cross-talk. However, a recent study did not support the evidence that the engulfed fibres can exchange either Na vs Ca or Na vs K, even though the same authors observed a significant decrease of cytoplasmic Ca^{2+} and concomitant increase of Na^+ [35]. This aspect is particularly relevant because several biochemical processes are regulated by chemical equilibria between Ca^{2+} and Na^+ across the cellular membrane [36–39]. More recently, a new study on erionite incubated in human THP-1 macrophages indicated, after phagocytosis, cations release counterbalanced by hydronium ions sequestration directly from lysosomes [40]. The effects included rapid pH dysregulation, hyperactivation of ATP-pumps, mitochondrial stress and chronic inflammation onset.

The contrasting results in the literature highlight that the involved mechanisms are more complex than expected and therefore need further investigation. Moreover, it is possible that different erionite species, classified based on of their dominant EF cation (K-, Ca-, or Na-erionite), show significant variations in toxic and carcinogen responses, as might other fibrous zeolites. To the best of our knowledge, the erionite samples investigated so far were Na- [28,31,34,35,40] or K-rich erionite [33,41], even though the fibres related to epidemic malignant mesothelioma are Ca-rich [42–43]. In this respect, the chemical composition of the pristine material is decisive for the reactions within the lungs. Based on these considerations, erionite-Ca was selected as testing material for the first time in this study. The present work aims to investigate, in *real-time* and at significant time intervals, erionite's chemical and structural modifications. Additionally, this study presents a novel comparative investigation involving two other fibrous zeolites — offretite and mordenite — aimed at elucidating differences and similarities in their behaviour with respect to erionite. Notably, exchange-data for offretite and mordenite in the lung environment is lacking, despite their potential dangerousness [10–12]. Most published studies characterize the structure of the fibres after incubation with pulmonary fluids using powder X-ray diffraction. However, in most cases, the powder material contains impurities such as clay minerals, oxides and other zeolites, which may interfere with the results. To avoid this, our experiments are performed on zeolite single crystals, which are used here for the first time to rule out possible interferences. Well-shaped crystals were selected and analysed before, during, and after interaction in Gamble's solution using Single-Crystal X-ray Diffraction (SC-XRD). The accurate chemical compositions of erionite, offretite, and mordenite samples were obtained by X-ray Energy Dispersive Scanning Electron Microscopy (SEM-EDX) and Electron Microprobe Analysis (EMPA).

2. Materials and methods

2.1. Zeolite samples and simulated lung fluid (SLF)

Three different zeolites were tested in the present study: erionite, offretite, and mordenite. The erionite sample (MB2404) is from Northern Ireland and has been previously investigated by Giordani and coauthors [32]. Offretite (MTS) comes from Mount Semiol, Loire, France, while the mordenite sample (labelled MOL1) is from Sardinia, Italy, and it was investigated from a mineralogical and toxicological point of view by Giordani and coauthors [44]. All natural samples were newly characterized in the present work using X-ray Energy Dispersive Scanning Electron Microscopy (SEM-EDX), Electron Microprobe Analysis (EMPA), and Single-Crystal X-ray Diffraction (SC-XRD). Chemical compositions and crystal structures of each sample were investigated after immersion in SLF, at different interaction times, with SEM-EDX and SC-XRD.

The SLF used for the experiments is the Gamble's solution, prepared following the method described by Rozalen and coauthors [45]. To simplify the system and avoid further interferences with the extra framework of zeolites, we prepared the solution with only two salts: NaCl (112.3 mmol/L, Sigma-Aldrich, ≥99.0%) and Na_2SO_4 (0.556 mmol/L, Sigma-Aldrich, ≥ 99%), maintaining the original salt concentration, as suggested by Pacella and coauthors [33]. HCl was added to reach a pH value of 4.5, which simulates the acidic environment of macrophage cells, as previously described [33] to enhance a process that occurs very slowly in vivo, in order to obtain experimental evidence of any changes within a reasonable experimental time. Furthermore, using the same conditions reported in previous studies, we were able to compare published results with those obtained in this work.

One crystal from each sample was glued on the tip of a glass fibre. The fibres were fixed on the vial's cap and immersed in the vial containing the SLF solution. The vials were kept at 37 °C throughout the experiments to simulate the body temperature. Each crystal was immersed in a separate vial with 10 ml of Gamble's solution, and the solution was replaced with fresh solution every 7 days. For the chemical characterization, several crystals of each sample were immersed in separated vials containing Gamble's solution and extracted at the selected interaction times. The extracted crystals were mounted on carbon tape holders for SEM-EDX investigation. Also for these samples, the solution was refreshed every 7 days. The selected interaction times were: 6 days (Time 1), 13 days (Time 2), 20 days (Time 3), 26 days (Time 4), 33 days (Time 5).

2.2. Chemical characterization of zeolite samples

Chemical analyses were performed using a Zeiss Gemini Sigma 560 VP scanning electron microscope (SEM) coupled with an EDX detector (Oxford Instruments Ultim-Max 170). Operating conditions were 10 keV accelerating voltage, 10 mm working distance, and 0° tilt angle. Chemical compositions represent average values obtained from at least 11 point analyses conducted on a minimum of three different crystals. In addition, the single crystals used for XRD measurements were also investigated by SEM-EDX after the end of the experiment (i.e. after one month of interaction). In the latter case, the measurements were performed for each zeolite at different crystal points.

UNCORRECTED PROOF

In order to minimize the alkali metal migration during measurements, a low counting time (10 s) and raster scan mode (to reduce the temperature increase) were adopted, as previously suggested [46,47]. Final crystal-chemical formulas were calculated by normalizing the chemical composition using an assumed water content of 18 wt% for erionite and offretite and 13 wt% for mordenite. The reliability of the chemical analyses was evaluated by using the charge balance error formula E% [48], along with the K-content test [12,49], and the Mg-content test [50].

For comparison, the natural samples (MB2404, MTS, MOL1) were also investigated by Electron Probe Microanalyser (EPMA) using a Jeol JXA-8200 WD/ED instrument. Crystals were embedded in epoxy resin, and chemical analyses were performed according to the recommended protocol by Campbell and coauthors [51]. Chemical data were collected on different crystals to assess homogeneity. The final chemical formulas were calculated as averages based on several analytical points across different crystals. Average compositions and details are reported respectively in Tables 1 and S1 for offretite, Tables 2 and S2 for mordenite, and Tables 3 and S3 for offretite. Representative SEM-EDX spectra of the samples (natural and at time 5) are reported in Fig. S1. Data's reliability was evaluated using the same tests used for SEM-EDX: charge balance error formula E%, K-content test, and Mg-content test. The crystal chemical formulas were calculated, after renormalization of chemical analyses based on oxygen counts of $O = 72$ for erionite, $O = 36$ for offretite, and $O = 96$ for mordenite.

2.3. X-Ray diffraction

Diffraction data of natural and interacted samples in Gamble's solution (from Time 1 to Time 5) were collected using a XtaLAB Synergy-R diffractometer, Rigaku Oxford Diffraction, equipped with a rotating anode (MoKα λ = 0.71073 Å) and a curved detector HyPix-Arc 100° A single crystal of each natural zeolite was glued on the top of a glass fibre and mounted onto a goniometer head. Additional crystals from each sample were glued on glass fibres and inserted in the vials with the SLF. These fibres with single crystals were extracted from the vials at selected interaction times and directly mounted on the goniometer head for XRD experiments. After each measurement, the samples were returned to the vials containing the SLF. In this way, the same single crystal could be monitored at the selected interaction time.

X-ray data were integrated and corrected for absorption using the software CrysAlisPro 1.171.43.144a [52]. Structures were solved by direct methods by Shelxt 2014 [53] and refined by Shelxl 2015 [54], using the software package WingX [55]. Cations were assigned based on the electron density peaks, bond-distances with oxygen of the framework and comparison with previous reported models in literature [56–58]. All structural drawings were produced by the software VESTA 2011 [59]. Crystal data, collection and refinement parameters are reported in Tables 4, 5, and 6, for offretite, mordenite, and erionite, respectively. The occupancy values are reported in Tables 7–9. Representative precession images of XRD measurements (natural and at time 5) are reported in Figs. S2, S3, and S4, respectively for offretite, mordenite, and erionite. CIF files of the investigated samples are available for download at the journal site.

Table 1
Average chemical compositions of the offretite (MTS) sample.

	EMPA	SEM-EDX						
MTS	Natural	Natural	Time 1	Time 2	Time 3	Time 4	Time 5	Time 5sc
Si	13.01	13.30	12.78	12.88	12.77	12.92	12.88	12.85
Al	5.00	4.69	5.24	5.10	5.18	5.10	5.13	5.20
Fe2 +	0.00	0.00	0	0	0	0	0	0
Mg	0.98	0.88	0.73	0.70	0.82	0.75	0.52	0.87
Ca	0.95	0.95	0.47	0.67	0.41	0.43	0.16	0.52
Ba		0.00	0	0	0	0	0	0
Na	0.01	0.00	1.79	1.23	1.93	1.68	2.60	1.29
K	1.10	1.08	0.98	1.20	0.97	0.98	1.14	0.87
H2O	15.37	14.35	14.53	14.56	14.54	14.49	14.62	14.44
E%	0.01	−0.73	1.43	−1.17	−3.35	1.67	0.59	4.26

Table 2
Average chemical compositions of the mordenite (MOL) sample.

	EMPA	SEM-EDX						
MOL1	Natural	Natural	Time 1	Time 2	Time 3	Time 4	Time 5	Time 5sc
Si	40.21	38.94	38.97	39.17	39.25	38.81	38.96	39.17
Al	7.86	9.17	9.12	8.86	8.83	9.26	9.16	8.86
Fe2 +	0.01	0	0	0	0	0	0	
Mg	0.01		0	0	0	0	0	0
Ca	2.04	2.33	1.83	1.54	1.81	1.88	1.73	1.04
Ba		0	0	0	0	0	0	0
Na	3.35	3.96	5.10	5.64	4.88	5.19	5.26	6.69
K	0.13	0.12	0	0	0	0	0	0
H2O	25.23	25.43	25.44	25.44	25.39	25.47	25.44	25.47
E%	0.04	4.98	4.17	1.61	4.05	3.49	5.14	1.23

Table 3
Average chemical compositions of the erionite (MB2404) sample.

	EMPA	SEM-EDX						
MB2404	Natural	Natural	Time 1	Time 2	Time 3	Time 4	Time 5	Time 5sc*
Si	26.47	25.99	25.70	25.91	26.24	26.38	25.97	25.38
Al	9.48	10.12	10.39	10.12	9.89	9.68	9.93	10.48
Fe2 +	0.05	0.00	0	0	0	0	0	0
Mg	0.31	0.04	0	0	0	0.03	0	0
Ca	3.39	3.70	0	0	0	0	0	0.53
Ba	0.00	0.00	0	0	0	0	0	0
Na	0.08	0.18	8.04	8.03	7.41	7.53	8.3	8.45
K	2.05	2.00	2.00	1.99	1.98	1.86	2.06	1.52
H2O	28.10	29.08	29.45	29.43	29.29	29.25	29.49	29.25
E%	−0.10	4.78	3.60	1.13	5.40	2.43	−3.96	−4.82

* Calculated by 5 point analyses.

3. Results and discussion

3.1. Pristine materials

The three samples were newly characterized by SC-XRD, SEM, and EMPA. The crystal structures of the three minerals were generally consistent with previous studies [56–58]. The chemical compositions of offretite (Table 1), mordenite (Table 2), and erionite (Table 3), determined by SEM, were found to be consistent with those obtained by EMPA.

In offretite (MTS) $(K_{1.08}Mg_{0.88}Ca_{0.95})(Al_{4.69}Si_{13.30}O_{36})\cdot 14\cdot 35H_2O$ (Table 1), Ca atoms are positioned at the C1 site, located along the 12-membered ring channels parallel to [001] (Fig. 1a). C1 lies in a split position above and below the mirror plane perpendicular to [001] with maximum occupancy equal to 0.5 (Table 7). It coordinates to 3 H_2O at W1 and 3 H_2O at W3 site (Fig. 1a). Mg atoms are located in the centre of the *gmelinite* cavity (*gme*) coordinated by H_2O, which are disorderly distributed in the *ab*-plane at W2 and W2A sites, and at the W4 site located on the 3-fold axis. K atoms are found inside the cancrinite cage (*can*), coordinated to framework oxygen atoms. Atom coordinates, atomic displacement parameters, and occupancy factors are reported in Table S4.

The natural mordenite (MOL1) has chemical composition $(Na_{2.96}Ca_{2.33}K_{0.12})[Al_{9.17}Si_{38.94}O_{96}]\cdot 25\cdot 43H_2O$ (Table 2). Na atoms fully occupy the C1 site, located along the 8-membered ring channel running parallel to [001]. Ca atoms are disorderly distributed across partially occupied sites (C2, C22, and C2A) located in the middle of the big 12-

UNCORRECTED PROOF

Table 4
Crystal data, collection and refinement parameters of offretite (MTS) at different interaction times.

Crystal data	Offretite time 1	Offretite time 2	Offretite time 3	Offretite time 4	Offretite time 5
a (Å)	13.2333(2)	13.2421(3)	13.2685(4)	13.2679(3)	13.225305(18)
c (Å)	7.57405(14)	7.57108(13)	7.5777(2)	7.57802(14)	7.57598(12)
V (Å^3)	1148.67(5)	1149.74(5)	1155.34(7)	1155.28(6)	1152.39(4)
Z	1	1	1	1	1
Space group	*P-6m2*	*P-6m2*	*P-6m2*	*P-6m2*	*P-6m2*
Refined chemical formula	$K_1Mg_1Na_{0.82}Ca_{0.18}(Si_{13.14}Al_{4.86}O_{36})\cdot 12.78H_2O$	$K_1Mg_1Na_{0.66}Ca_{0.34}(Si_{13.14}Al_{4.86}O_{36})\cdot 12.99H_2O$	$K_1Mg_1Na_{0.37}Ca_{0.63}(Si_{13.14}Al_{4.86}O_{36})\cdot 14.46H_2O$	$K_1Mg_1Na_{0.4}Ca_{0.60}(Si_{13.14}Al_{4.86}O_{36})\cdot 13.99H_2O$	$K_1Mg_1Na_{0.73}Ca_{0.27}(Si_{13.14}Al_{4.86}O_{36}$
Crystal size (mm)	0.340 × 0.130 × 0.100	0.340 × 0.130 × 0.100	0.340 × 0.130 × 0.100	0.340 × 0.130 × 0.100	0.340 × 0.130 × 0.100
Data collection					
Diffractometer	XtaLAB Synergy R, HyPix-Arc 100	XtaLAB Synergy R, HyPix-Arc 100	XtaLAB Synergy R, HyPix-Arc 100	XtaLAB Synergy R, HyPix-Arc 100	XtaLAB Synergy R, HyPix-Arc 10
X-ray radiation	Mo$K\alpha$, λ = 0.71073 Å	Mo$K\alpha$, λ = 0.71073 Å	Mo$K\alpha$, λ = 0.71073 Å	Mo$K\alpha$, λ = 0.71073 Å	Mo$K\alpha$, λ = 0.71073 Å
Temperature (°C)	299(2)	299(2)	299(2)	293(2)	293(2)
Total time	14 m 2s	12 m 37s	4 m 1s	12 m 18s	16 m 36s
Max. 2θ (°)	75.83	75.64	75.35	71.03	70.88
Index ranges	$-20 \le h \le 22$ $-17 \le k \le 22$ $-13 \le l \le 10$	$-22 \le h \le 20$ $-22 \le k \le 21$ $-12 \le l \le 12$	$-16 \le h \le 20$ $-20 \le k \le 20$ $-10 \le l \le 11$	$-17 \le h \le 21$ $-21 \le k \le 20$ $-11 \le l \le 12$	$-21 \le h \le 21$ $-20 \le k \le 21$ $-12 \le l \le 12$
No. of measured reflections	18,252	15,865	12,455	15,558	37,189
No. of unique reflections	2345	2310	1836	1873	2010
No. of observed reflections $I > 2\sigma$ (I)	2214	2161	1664	1791	1925
Structure refinement					
No. of parameters used in the refinement	87	87	82	82	84
R(int)	0.0247	0.0297	0.0324	0.0266	0.0292
$R(\sigma)$	0.0156	0.0193	0.0235	0.0159	0.0109
GooF	1.081	1.296	1.061	1.062	1.107
$R1$, $I > 2\sigma$ (I)	0.0339	0.0374	0.0370	0.0334	0.0339
$R1$, all data	0.0360	0.0399	0.0414	0.0349	0.0354
$wR2$ (on F^2)	0.1011	0.1156	0.1065	0.0999	0.0999
$\Delta\rho_{min}$ (-eÅ^{-3}) close to	−0.90 Mg	−0.86 Mg	−0.79 Mg	−0.76 Mg	−0.99 Mg
$\Delta\rho_{max}$ (eÅ^{-3}) close to	0.64 W1	0.65 W1	0.58 W4	0.60 W1	0.69 W1

UNCORRECTED PROOF

Table 5
Crystal data, collection and refinement parameters of mordenite (MOL) at different interaction times.

Crystal data	Mordenite time 1	Mordenite time 2	Mordenite time 3	Mordenite time 4	Mordenite time 5
a (Å)	18.0816(5)	18.0538(5)	18.0625(6)	18.0690(5)	18.0722(5)
b (Å)	20.4344(5)	20.4110(5)	20.4252(6)	20.4286(5)	20.4102(6)
c (Å)	7.5228(2)	7.51706(16)	7.5220(2)	7.51987(18)	7.51752(19)
V (Å^3)	2779.58(12)	2770.00(12)	2775.11(14)	2775.77(13)	2772.88(13)
Z	1	1	1	1	1
Space group	*Cmcm*	*Cmcm*	*Cmcm*	*Cmcm*	*Cmcm*
Refined chemical formula	$Na_{6.50}Ca_{1.02}(Si_{38.4}Al_{9.6}O_{96})\cdot 27.6H_2O$	$Na_{6.24}Ca_{0.72}(Si_{38.4}Al_{9.6}O_{96})\cdot 26.24H_2O$	$Na_{6.4}Ca_{0.85}(Si_{38.4}Al_{9.6}O_{96})\cdot 26.24H_2O$	$Na_{6.34}Ca_{0.92}(Si_{38.4}Al_{9.6}O_{96})\cdot 25.96H_2O$	$Na_{6.67}Ca_{0.61}(Si_{40.8}Al_{7.2}O_{96})\cdot 25.88H_2O$
Crystal size (mm)	0.383 × 0.050 × 0.020	0.383 × 0.050 × 0.020	0.383 × 0.050 × 0.020	0.383 × 0.050 × 0.020	0.383 × 0.050 × 0.020
Data collection					
Diffractometer	XtaLAB Synergy R, HyPix-Arc 100	XtaLAB Synergy R, HyPix-Arc 100	XtaLAB Synergy R, HyPix-Arc 100	XtaLAB Synergy R, HyPix-Arc 100	XtaLAB Synergy R, HyPix-Arc 100
X-ray radiation	Mo$K\alpha$, λ = 0.71073 Å	Mo$K\alpha$, λ = 0.71073 Å	Mo$K\alpha$, λ = 0.71073 Å	Mo$K\alpha$, λ = 0.71073 Å	Mo$K\alpha$, λ = 0.71073 Å
Temperature (°C)	299(2)	299(2)	299(2)	299(2)	299(2)
Total time	25 m 21s	18 m 12s	17 m 0s	21 m 59s	15 m 27s
Max. 2θ (°)	75.73	75.86	70.73	70.85	70.73
Index ranges	$-30 \le h \le 30$	$-30 \le h \le 29$	$-29 \le h \le 21$	$-28 \le h \le 16$	$-24 \le h \le 28$
	$-34 \le k \le 34$	$-34 \le k \le 34$	$-19 \le k \le 32$	$-31 \le k \le 31$	$-32 \le k \le 31$
	$-7 \le l \le 12$	$-12 \le l \le 12$	$-10 \le l \le 11$	$-11 \le l \le 11$	$-11 \le l \le 11$
No. of measured reflections	19,727	19,629	15,547	15,600	12,423
No. of unique reflections	3881	3895	3144	3163	3166
No. of observed reflections $I > 2\sigma$ (I)	3128	3111	2657	2654	2616
Structure refinement					
No. of parameters used in the refinement	141	130	130	131	126
R(int)	0.0245	0.0243	0.0202	0.0194	0.0230
R(σ)	0.0205	0.0210	0.0175	0.0181	0.0232
GooF	1.068	1.065	1.056	1.095	1.075
$R1$, $I > 2\sigma$ (I)	0.0455	0.0502	0.0489	0.0487	0.0499
$R1$, all data	0.0553	0.0605	0.0564	0.0565	0.0580
$wR2$ (on F^2)	0.1579	0.1772	0.1652	0.1689	0.1721
$\Delta\rho_{min}$ (-eÅ^{-3}) close to	−0.77 W2	−1.16 W3A	−1.05 W2	−1.12 W2	−1.03 W2
$\Delta\rho_{max}$ (eÅ^{-3}) close to	1.06 W1	0.95 O5	0.88 W4	0.92 O5	0.96 C3

UNCORRECTED PROOF

Table 6
Crystal data, collection and refinement parameters of erionite (MB2404) at different interaction times.

Crystal data	Erionite time 1	Erionite time 2	Erionite time 3	Erionite time 4	Erionite time 5
a (Å)	13.2551(3)	13.2338(4)	13.2421(4)	13.2404(4)	13.2460(5)
c (Å)	15.2174(3)	15.1900(4)	15.2073(4)	15.1949(4)	15.2188(4)
V (Å^3)	2315.47(13)	2303.86(15)	2309.38(14)	2306.93(15)	2312.5(2)
Z	1	1	1	1	1
Space group	$P6_3/mmc$	$P6_3/mmc$	$P6_3/mmc$	$P6_3/mmc$	$P6_3/mmc$
Refined chemical formula	$Na_{7.74}K_{2.02}(Si_{25.80}Al_{10.2})O_{72}{\cdot}11.13H_2O$	$Na_{7.50}K_{2.01}(Si_{25.80}Al_{10.2})O_{72}{\cdot}11.23H_2O$	$Na_{7.48}K_{2.01}(Si_{25.80}Al_{10.2})O_{72}{\cdot}11.20H_2O$	$Na_{7.67}K_2(Si_{25.80}Al_{10.2})O_{72}{\cdot}11.38H_2O$	$Na_{7.42}K_2(Si_{25.80}Al_{10.2})O_{72}{\cdot}11.27H_2O$
Crystal size (mm)	0.170 × 0.045 × 0.030	0.170 × 0.045 × 0.030	0.170 × 0.045 × 0.030	0.170 × 0.045 × 0.030	0.170 × 0.045 × 0.030
Data collection					
Diffractometer	XtaLAB Synergy R, HyPix-Arc 100	XtaLAB Synergy R, HyPix-Arc 100	XtaLAB Synergy R, HyPix-Arc 100	XtaLAB Synergy R, HyPix-Arc 100	XtaLAB Synergy R, HyPix-Arc 100
X-ray radiation	Mo$K\alpha$, λ = 0.71073 Å	Mo$K\alpha$, λ = 0.71073 Å	Mo$K\alpha$, λ = 0.71073 Å	Mo$K\alpha$, λ = 0.71073 Å	Mo$K\alpha$, λ = 0.71073 Å
Temperature (°C)	299(2)	299(2)	297(2)	297(2)	297(2)
Total time	2 h 9 m 17s	2 h 51 m 15s	2 h 51 m 5s	2 h 40 m 34s	2 h 53 m 54s
Max. 2θ (°)	61.01	61.01	61.00	61.01	60.99
Index ranges	$-18 \le h \le 15$	$-12 \le h \le 18$	$-14 \le h \le 18$	$-18 \le h \le 14$	$-18 \le h \le 18$
	$-18 \le k \le 16$	$-18 \le k \le 12$	$-15 \le k \le 18$	$-18 \le k \le 18$	$-18 \le k \le 17$
	$-21 \le l \le 21$	$-21 \le l \le 21$	$-21 \le l \le 18$	$-20 \le l \le 21$	$-21 \le l \le 13$
No. of measured reflections	18,742	18,639	13,994	18,536	16,444
No. of unique reflections	1369	1361	1366	1364	1367
No. of observed reflections $I > 2\sigma$ (I)	1219	1243	1088	1230	1169
Structure refinement					
No. of parameters used in the refinement	86	85	86	84	82
R(int)	0.0612	0.0510	0.0691	0.0559	0.0689
$R(\sigma)$	0.0286	0.0253	0.0376	0.0290	0.0369
GooF	1.325	1.321	1.203	1.309	1.338
$R1$, $I > 2\sigma$ (I)	0.0929	0.0802	0.0821	0.0849	0.1004
$R1$, all data	0.1051	0.1051	0.1075	0.0958	0.1167
$wR2$ (on F^2)	0.1854	0.1726	0.1777	0.1816	0.2167
$\Delta\rho_{min}$ (-eÅ^{-3}) close to	−0.87 C1	−0.57 C1	−0.60 C1	−0.59 C1	−0.87 C1B
$\Delta\rho_{max}$ (eÅ^{-3}) close to	0.82 C3	0.73 W1	0.78 W1	0.72 W1	0.84 C3

UNCORRECTED PROOF

Table 7
Site occupancy of offretite (MTS).

Occupancy		OFF NAT	time 1	time 2	time 3	time 4	time 5
Si1		0.73	0.73	0.73	0.73	0.73	0.73
Al1		0.27	0.27	0.27	0.27	0.27	0.27
Si2		0.73	0.73	0.73	0.73	0.73	0.73
Al2		0.27	0.27	0.27	0.27	0.27	0.27
O1		1	1	1	1	1	1
O2		1	1	1	1	1	1
O3		1	1	1	1	1	1
O4		1	1	1	1	1	1
O5		1	1	1	1	1	1
O6		1	1	1	1	1	1
C1	Na		0.42(2)	0.33(2)	0.18(3)	0.20(3)	0.37(3)
	Ca	0.5	0.08(2)	0.17(2)	0.32(3)	0.30(3)	0.13(3)
K		1	1	1	1	1	1
Mg		1	1	1	1	1	1
W1		1	0.64(4)	0.65(4)	1	1	1
W1A			0.22(3)	0.17(3)			
W2		0.36(3)	0.42(2)	0.41(3)	0.49(3)	0.45(2)	0.39(2)
W2A		0.33(2)	0.348(19)	0.35(2)	0.35(2)	0.331(19)	0.321(19)
W2B		0.30(4)	0.23(3)	0.30(4)	0.26(4)	0.32(4)	0.23(4)
W3		0.73(4)	0.69(4)	0.73(5)	0.82(5)	0.80(4)	0.81(4)
W4		0.95(3)	0.94(2)	0.92(2)	0.96(3)	0.96(3)	0.95(3)
W4A		0.07(3)	0.11(3)	0.08(3)			0.10(3)

Table 8
Site occupancy of mordenite (MOL).

Occupancy	MOL NAT	time 1	time 2	time 3	time 4	time 5
Si1	0.8	1	1	1	1	0.8
Al1	0.2					0.2
Si2	0.8	0.7	0.7	0.7	0.7	0.8
Al2	0.2	0.3	0.3	0.3	0.3	0.2
Si3	0.5	0.4	0.4	0.4	0.4	0.5
Al3	0.5	0.6	0.6	0.6	0.6	0.5
Si4	1	1	1	1	1	1
O1	1	1	1	1	1	1
O2	1	1	1	1	1	1
O3	1	1	1	1	1	1
O4	1	1	1	1	1	1
O5	1	1	1	1	1	1
O6	1	1	1	1	1	1
O7	1	1	1	1	1	1
O8	1	1	1	1	1	1
O9	1	1	1	1	1	1
O10	1	1	1	1	1	1
C1	0.986(8)	0.988(9)	0.983(10)	0.986(11)	0.989(11)	1
C2	0.029(13)	0.044(15)	0.043(12)	0.034(13)	0.033(11)	
C22	0.035(6)					
C2A	0.200(6)	0.637(11)	0.577(10)	0.613(18)	0.597(11)	0.655(11)
C3	0.124(9)	0.106(8)	0.068(7)	0.09(9)	0.098(10)	0.075(8)
W1	1	1	1	1	1	1
W2	1	1	1	1	1	1
W2A	0.169(10)	0.149(10)	0.166(10)	0.136(10)	0.160(11)	0.156(11)
W2B	0.092(7)	0.090(8)				
W3	0.42(6)	0.53(7)	0.27(3)	0.31(6)	0.29(5)	0.73(8)
W3A	0.51(2)	0.44(3)	0.594(17)	0.53(3)	0.56(2)	0.36(3)
W4	0.23(3)	0.25(3)	0.78(4)	0.75(4)	0.76(4)	0.72(4)
W4A	0.335(16)	0.292(16)				

membered ring channel, and in the adjacent *t-mor** cavity at the C3 site (Table 8; Fig. 2a). H_2O are distributed at four main sites (W1, W2, W3, W4), which are affected by positional disorder. Atom coordinates, atomic displacement parameters, and occupancy factors are reported in Table S5.

The SEM analyses of the erionite sample (MB2404) were consistent with those obtained by EMPA, leading to the calculated chemical formula: $(Ca_{3.70}K_{2.00}Mg_{0.04}Na_{0.18})[Al_{10.12}Si_{25.99}O_{72}]\cdot 29{\cdot}08H_2O$ (Table 3). Structural refinement on data sets from different crystal fragments consistently showed that the EF cations distribution within the *eri* cavity differs from that of our previous study, where Ca atoms were mostly located at the C1 and C2 sites [32]. In contrast, the new data highlight that the most occupied sites are C3 occ. = 0.444(10) and C2 occ. = 0.273 (15), while the residual Ca is disorderly distributed at C1, C1A, and C1B (total occ. = 0.296) (Fig. 3a; Table 9). These latter sites are located in the middle of the *eri* cavity, in the proximity of the W5 site, which, in our previous refinement, was occupied by H_2O. The distribution of different EF cations obviously affects the location of the H_2O sites. W2, W3, and W3A bond to the C1 sites, additional water is located at W4, and W4A is in the middle of the 8mr window of the *eri* cavity (Fig. 3a). Atom coordinates, atomic displacement parameters, and occupancy factors are reported in Table S6.

Table 9
Site occupancy of erionite (MB2404).

occupancy	ERI NAT	time 1	time 2	time 3	time 4	time 5
Si1	0.66	0.66	0.66	0.66	0.66	0.66
Al1	0.34	0.34	0.34	0.34	0.34	0.34
Si2	0.83	0.83	0.83	0.83	0.83	0.83
Al2	0.17	0.17	0.17	0.17	0.17	0.17
O1	1	1	1	1	1	1
O2	1	1	1	1	1	1
O3	1	1	1	1	1	1
O4	1	1	1	1	1	1
O5	1	1	1	1	1	1
O6	1	1	1	1	1	1
K	1	0.985(18)	0.988(17)	0.990(17)	0.9799	1
K1A		0.014(8)	0.009(7)	0.010(7)	0.0049	
C1	0.109(8)	0.277(19)	0.288(17)	0.261(16)	0.277(18)	0.27(2)
C1A	0.085(6)	0.106(15)	0.103(13)	0.080(12)	0.106(14)	0.086(16)
C1B	0.102(6)	0.068(19)	0.062(17)	0.063(17)	0.066(19)	0.06(2)
C1C		0.173(16)	0.162(14)	0.158(14)	0.173(15)	0.173(19)
C2	0.273(15)	0.36(4)	0.34(4)	0.33(4)	0.35(4)	0.35(5)
C3	0.444(10)	0.76(3)	0.74(3)	0.76(3)	0.74(3)	0.75(4)
W1		0.29(4)	0.32(3)	0.26(3)	0.28(4)	0.17(4)
W1A		0.22(4)	0.16(3)	0.16(3)	0.22(3)	0.34(4)
W2	0.259(15)					
W3	0.280(16)	0.43(3)	0.46(3)	0.47(3)	0.45(3)	0.43(4)
W3A	0.39(4)					
W4	0.375(16)					
W4A	0.27(2)					

The observed structural differences, and the lower amount of Mg content reported by the chemical analyses compared to our previous investigation are ascribed to the presence of offretite stacking-faults in the crystal measured by [32]. In the present study, none of the analysed crystals showed electron density that could be associated with residual Si or O from offretite faults, effectively ruling out their presence.

3.2. Interaction with simulated lung fluid

Offretite (MTS). Chemical analyses of offretite at different interaction times show a general decrease in Ca content and an increase in Na (Table 1, Table S1, Fig. S1). The Na uptake rises from 1.79 to 2.6 apfu, from times 1 and 5, respectively. Some fluctuations in the Ca/Na trend are partially ascribed to the chemical variability among the analysed crystals, although structural refinements consistently confirm the same compositional trend. The Na content at different interaction times varies inversely with Ca, confirming that Na substitutes Ca during the exchange process. In contrast, Mg and K contents remain unaffected by the fluid interaction. At time 1, a pronounced decrease in the site scattering (ss) of C1, along with a reduction in unit-cell volume, points to the incorporation of a lighter and smaller cation (Table 7). In agreement with the chemical analyses, the C1 site (i.e., the only site hosting Ca atoms) is affected by significant changes in the site scattering. Therefore, C1 occupancy was refined using mixed Ca and Na scattering curves. The refinement converged to a total occupancy of 0.5 apfu corresponding to 0.08 Ca and 0.42 Na apfu (Fig. 1b, Table 7). Although the good quality of the structural refinement, this leads to an unbalanced refined chemical composition, with a defect of positive charges

UNCORRECTED PROOF

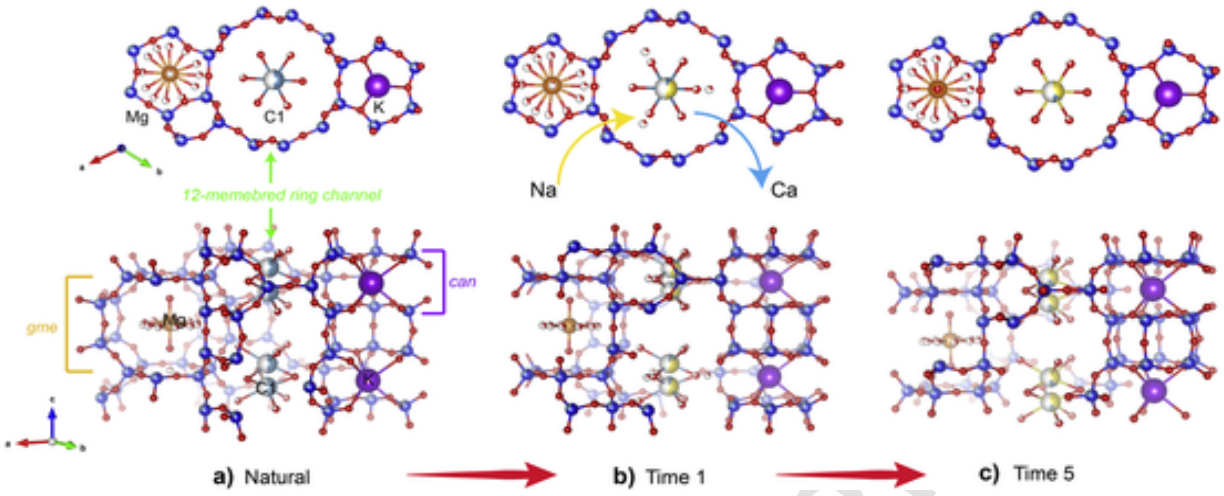

Fig. 1. Perspective view of the crystal structure of offretite (MTS) projected along [001] and [110]. The silicoaluminate framework is represented by blue (Si/Al) and red spheres (O). (a) Crystal structure of natural offretite showing the gmelinite and cancrinite cavities, as well as the 12-memebred ring channel. The extra framework cations are labeled according to sites name: Ca is represented in dark cyan, Mg in orange, K in purple, and Na in yellow. Partial occupancy of the refined sites is shown by partially colored spheres. Structure of offretite after 1 week (b) and five weeks (c) of interactions with SLF.

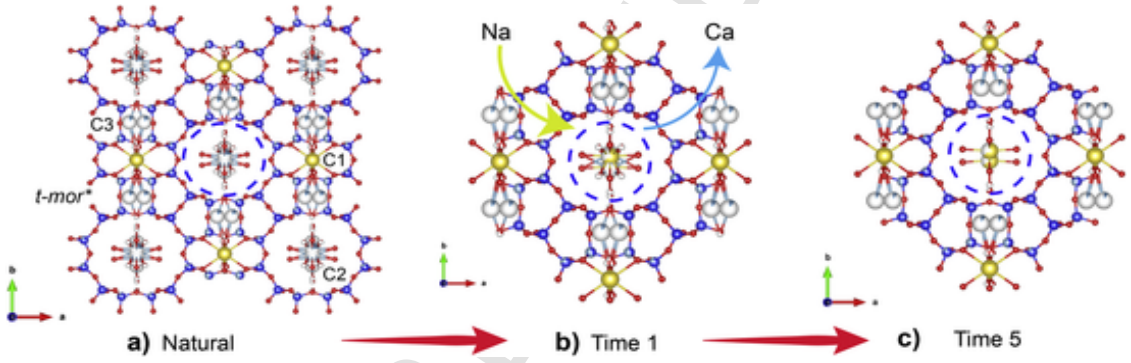

Fig. 2. Crystal structure of mordenite (MOL1) projected along [001], at natural conditions (a), time 1 (b), and time 5 (c) of interaction with SLF. Color code as in Fig. 1. The dashed blue circle highlights the 12-membered ring channel parallel to [001], where most of the Na replaces Ca during the interaction with SLF.

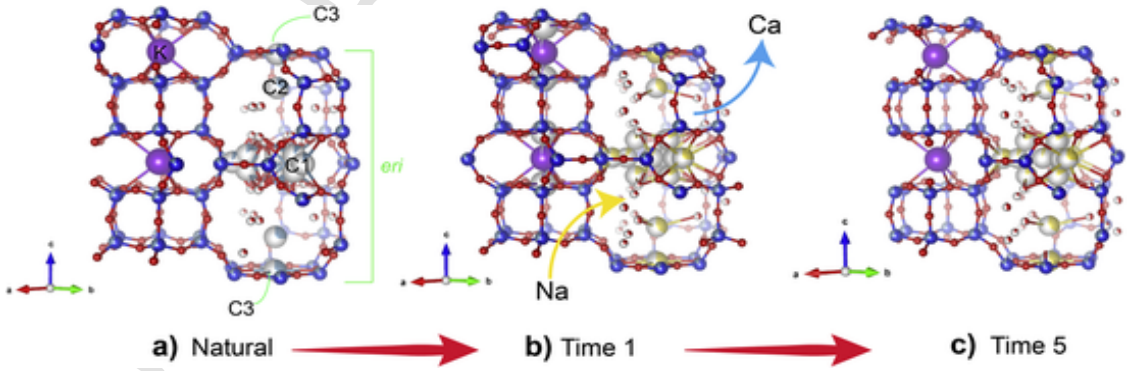

Fig. 3. Perspective view of the crystal structure of erionite (MB2404) projected along [110], at natural conditions (a), time 1 (b), and time 5 (c) of interaction with SLF. The extra framework cations are labeled according to sites name. Color code as in Fig. 1.

due to the Ca^{2+}-> Na^{+} substitution. In addition, no evidence was found for: i) peaks in difference Fourier maps, suggesting the presence of additional EF sites, which might be potentially occupied by residual Na; ii) variations in the occupancy or coordination of the H_2O sites, which might host additional Na.

The same scenario was observed in the structure obtained at subsequent interaction times (Fig. 1c, Tables S). Overall, i) refinements considering only Ca at C1 site resulted in a net decrease of the site scattering factor; ii) refinements carried out by using mixed scattering curves (i.e. Ca vs Na) lead to an unbalanced chemical formula, with an excess of negative charges; iii) the chemical variations observed throughout the incubation period (from time 1 to time 5) were consistently reproduced by the refined chemical composition (Fig. 4). At present, it remains unclear whether additional Na is located at surface sites or whether the lack of positive charges is compensated by the presence of protons attached to framework oxygen atoms.

Mordenite (MOL1). The observed trend in mordenite is in line with the other samples, albeit with differences. A significant increase of Na content (from 3.96 to 5.10 apfu), and a corresponding decrease of Ca (from 2.33 to 1.83 apfu) occur already at time 1. Similar to what was observed in offretite, although to a lesser extent, the trend of the chemical composition is characterized by slight oscillations during the interaction time. However, Ca is never fully replaced by Na. At time 5, the total Ca and Na contents are 1.73 and 5.26 apfu, respectively (Table 2; Table S2, Fig. S1).

Structural refinements showed that, among the EF cation sites, the most affected is C2A, whose occupancy factor varies significantly over time. Ca at C2A (sof = 0.200(6)) in the pristine material is replaced by Na (sof = 0.637(11)) at time 1 (Table 8). This refined value remains approximately constant up to the end of the experiment. The H_2O slightly rearranged its distribution over the partially occupied sites, as demonstrated by minor variations in the sof values of the W4, W3 and W4A sites.

Erionite (MB2404). Chemical analyses performed on erionite interacted at different times with the SLF showed a complete release of Ca (from 3.70 to 0 apfu) already at time 1 (i.e., after one week). No Ca was detected up to the end of the experiment (time 5). Accordingly, Na content strongly increases at time 1, from 0.18 in the natural sample to 8.04 apfu (Table 3; Table S3, Fig. S1). Slight variations of K and Na content observed in the immersed crystals from time 1 to time 5 are within 1σ and are not significant. Notably, a Ca content of 0.53 apfu was determined in the single crystal used for the XRD measurements. This finding is quite surprising, since no Ca was detected in any of the other crystal fragments immersed in the solution during the entire experiment. We hypothesize that the incomplete Na-exchange, observed only on the single crystal used for SC-XRD, might be caused by the different type of crystal-solution exposure. In the multi-crystals/solution setup, fragments are fully immersed and in contact with the liquid, facilitating cation exchange. By contrast, the single crystal was glued on one side to the glass fibre, which might hinder or slow down the cation diffusion during the exchange process. Additionally, the chemical analyses obtained on the single crystal are all affected by a low K content (on average 1.52 apfu), indicating that the chemical data in this case are less reliable than those obtained from the crystal fragments [26]. The structural refinements indicated that the entering Na atoms locate at the same EF sites (i.e. C3, C2 and C1) occupied by Ca in the pristine material, without significant differences in terms of atomic coordinates. The H_2O slightly rearranges at W1, W1A and W3. These sites are closely spaced, pointing to the disorder of the water molecules, which link C2 and C1 sites between two *eri* cavities (Fig. 3). Potassium remains unaffected by the exchange process, as expected and usually reported for this large cation residing in the cancrinite cage [49]. Nevertheless, at interaction times 1,2,3, and 4, residual electron density was observed near the K site (Table 9). This was modelled by inserting an additional site (K1A), refined with K scattering factors occ. = 0.014 (8). No significant differences are observed in EF cations-position at time 2, 3, 4, and 5, indicating that, under these experimental conditions, the exchange process can be considered "equilibrated" after one week of interaction.

The interaction experiments showed that the three fibrous zeolites behave similarly when in contact with the simulated lung-fluid. Overall, the zeolites uptake most of the Na from the solution within the first week of interaction, and prolonging the time has no significant additional effects. Moreover, in all investigated samples, the R value (R = Si/Si + Al) remained constant throughout the experiment (Tables S1–S3), meaning that little to no dealumination process took place, as also observed in a previous study performed on erionite powder [31].

In the three investigated zeolites, cation exchange occurs via Ca replacement by Na ions in the solution. As observed in erionite, offretite does not release Mg or K, because these two cations are located inside

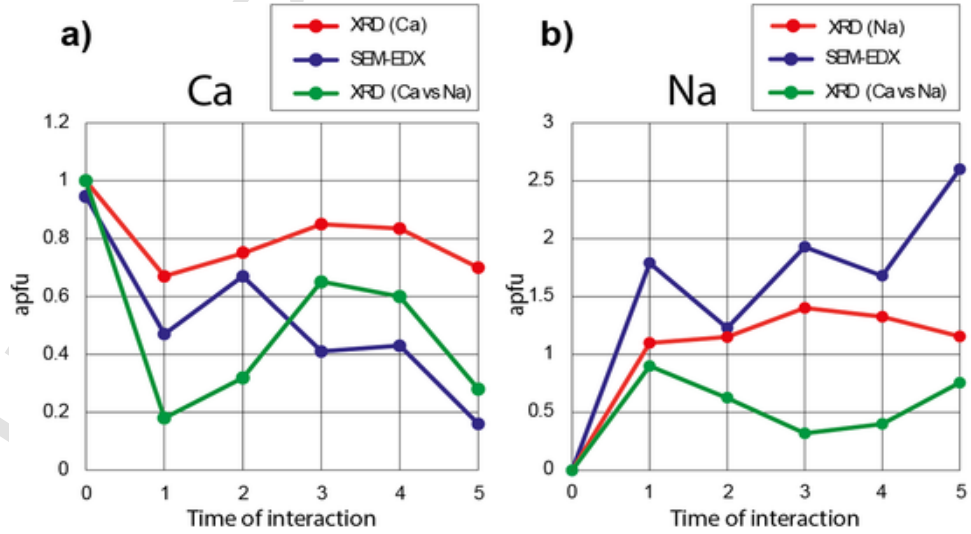

Fig. 4. Ca and Na apfu of offretite obtained from structural refinement (XRD) and from chemical analyses (SEM-EDX). Red curve shows the apfu content obtained by refining C1 site using only Ca (a) or Na (b) scattering factors. Green curve reports the Ca (a) and Na (b) amounts by refining the C1 site by using mixed scattering curves.

the *gmelinite* and *cancrinite* cage, respectively, which are more difficult to access (Fig. 1). Thus, fibrous offretite would similarly release Ca inside the lung environment if inhaled. The same applies to mordenite, which releases all available Ca, i.e., the one located in the large 12-membered ring channels, within 5 weeks of interaction.

This exchange process is consistent with what expected for erionite and mordenite, based on structural factors (i.e., interconnectivity of their pores and channels) and previous studies on their cation exchange capacity [31,60]. More intriguing is the case of offretite, for which the exchange capacity in aqueous solutions has been reported so far only for offretite synthesized with TMA template [61]. Under the applied experimental conditions, cations at C1 (i.e. in the centre of the big 12-membered ring channels) are those affected by the exchange process. However, the exact substitution mechanism remains unclear. Despite the high quality of the data and structural refinements, the resulting chemical formula remains unbalanced, exhibiting a deficiency in positive charges. As we stated before, it is unclear how the offretite structure compensates for this charge imbalance (i.e., additional Na at the surface, or presence of H^+). This issue is particularly significant because proton incorporation increases the acidity of the zeolite, thereby enhancing its chemical reactivity. In the lung environment, increased reactivity of the inhaled particles can be a critical factor in triggering carcinogenic reactions [38,62]. Some authors addressed to a small charge unbalance, resulted from minor EF cation release in SLF, the contribution of protonation of oxygen atoms of the framework, resulting in OH groups having the potential to act as a Brønsted acid sites [41]. However, this mechanism is unlikely in the presence of a large charge mismatch without loss of crystallinity, as suggested by Ballirano and coauthors [40].

Despite the general trend, the substitution mechanism in offretite could be more complex than initially hypothesized. The slight variations in the cation content observed as a function of time (Table 2) could, in principle, be related to chemical variability and inhomogeneity of the different fragments investigated by SEM-EDX. On the other hand, a comparable trend is confirmed by XRD data, which were collected on the exact same single crystal for the entire study. Fig. 4 compares the amount of Ca (Fig. 4a) and Na (Fig. 4b) obtained from structural refinements as a function of time with those estimated by the SEM-EDX analyses. The following cases were considered in each graph: i) C1 sof refined by using either Ca- or Na-scattering curves; ii) C1 refined by mixed scattering curves, i.e., Ca vs Na. Interestingly, a similar process was also observed on erionite after 48 h of leaching in SLF, where a transient Ca uptake was followed by Na reacquisition [31]. In this case, the authors attributed this behaviour to unwanted pH deviations from 7.4 after long-term CO_2 diffusion, the appearance of amorphous material and minor precipitation of calcium carbonate. The interpretation of such behaviour should consider that cation exchange is actually a dynamic process, rather than a simple unidirectional substitution of ions. In this context, the exchange should be viewed as a continuous equilibrium between the ions in solution and those within the zeolite structure. This dynamic nature suggests that cations could be mutually replaced through repeated cycles of adsorption and desorption during the interaction period, rather than in a single event.

This behaviour could also be related to retention or precipitation mechanisms, in which cations temporarily accumulate near or within the zeolite cages. These ions can form loosely bound or partially hydrated complexes at surface sites, which can subsequently be resorbed or replaced depending on changes in concentration, ionic strength, or local structural rearrangements. Consequently, the overall exchange process represents a balance between kinetic and thermodynamic factors, in which ionic mobility, hydration energy, and structure flexibility all play essential roles in determining the efficiency and selectivity of cation adsorption.

3.3. Comparison with previous experiments on erionite

Cation exchange processes occurring in erionite upon contact with simulated lung fluids have been investigated by several authors [31–34]. To the best of our knowledge, the chemical composition of all erionite fibres previously examined in studies on lung-fluid interactions differs from that of the Ca-rich erionite found in Tuzköy, Turkey [42,43], a locality where lung diseases have been unequivocally associated with this mineral. The only exception is the erionite sample analyzed by Giordani and coauthors [32], who, however, focused primarily on the chemical modifications at the mineral surface. In this context, it is worth emphasizing that the present experiments were conducted on erionite-Ca, which more accurately represents the composition of fibres implicated in the onset of pulmonary diseases such as *malignant mesothelioma* [63,64].

It is well established that the chemical composition of the pristine material can be a decisive factor in determining the reactions occurring within the lungs. Chemical composition, for example, is strongly linked to fibre bio-persistence and carcinogenic mechanisms, in which iron and trace elements play a significant role [65–67]. In the case of erionite fibres, the extent to which the dominant EF cation contributes to the development of lung disease mechanisms remain uncertain. Therefore, even limited variability in chemical and physical features, such as local compositional differences, may be relevant and should be taken into account.

In a previous study on erionite-Na in contact with ALF solution (Na-rich, pH = 4.5), the authors reported progressive Na^+ migration from Ca1 to Ca2 and to alternative sites associated with water molecules, ultimately leading to a Mg^{2+} segregation at Ca1 and Na^+ at Ca2 [31]. Similarly, in erionite-K, a marked replacement of Ca by Na was observed after one hour of interaction with the lung fluid (pH = 4.5) [33], followed by a complete Ca/Na exchange after one month. Structural investigations in the same study suggested a partial redistribution of cations toward positions previously occupied by H_2O within the erionite cage [33]. The observed decrease of s.s. at Ca1 (containing Mg and Na) and Ca3 (Ca), coupled with an increase at Ca2 (Na), was interpreted as evidence of Na migration toward Ca2, cation redistribution within the erionite cage (s.s. decrease at Ca1), and Ca release (s.s. decrease at Ca3). In the present study, cation redistribution at water sites was not observed. The incoming Na mainly locates at the same crystallographic positions (C1, C2, C3) previously occupied by Ca. The C2 site identified in this work corresponds approximately to the Ca2 position reported by Pacella and coauthors [33], whereas the C3 site (this work), positioned at the 6-membered ring window of the erionite cage, is empty in their sample. Furthermore, the K1 site described by Pacella and coauthors [33], which reflects the higher K content of their material, is occupied by H_2O in our sample. Table 10 presents a comparative summary of the principal observations reported in the literature and those derived from the present investigation.

A further important improvement of the present study lies in the ability to exclude the influence of minor phases and impurities on the cation exchange mechanism in SLF. Accessory phases are commonly associated with natural zeolites and are difficult to eliminate in powder samples, whereas single-crystal XRD provides superior data quality.

However, the crystals investigated here (elongated prisms rather than thin fibrils) are not respirable, representing a simplification of the system that nevertheless allowed the investigation of pure mineral phases. Other aspects are thus only approximated; for instance, the rate of cation exchange in thin fibrils, which have a higher specific surface area, would likely be greater. Finally, given the different chemical composition of the erionite examined in this work (Ca-rich), it is noteworthy that Ca ions are rapidly exchanged with Na from Gamble's solution, quickly converting the material to erionite-Na. Therefore, while the EF composition of natural erionite may influence its activity, this effect is probably limited to the early stages of interaction.

UNCORRECTED PROOF

Table 10
Summary of the main results obtained on erionite-exchange processes, as reported in literature and in the present study.

	Erionite	pH	rate of exchange	final Na content	cation site redistribution
[31] Ballirano and Cametti	eri-Na	4,5	Marginal modifications after 48 h and 4 months	4.49 apfu after 48 h, 4.22 apfu after 4 months	Segregation of Mg2+ at Ca1, migration of Na+ from Ca1 to Ca2 and toward sites located near the water molecule sites
[33] Pacella et al., 2021	eri-K	4,5	Significant replacement of Ca by Na in 1 h, full replacement in 1 month	3.06 apfu after 1 h, 3.75 apfu after 1 month	Increase of Na+ at Ca2, redistribution of Mg2+ and Na+ at Ca1, decrease of Ca2+ at Ca3. Partial redistribution of cations to position previously occupied by H2O in erionite cage
Present work	eri-Ca	4,5	Full replacement of Ca by Na in 1 week	8.04 apfu after 1 week, 8.30 apfu afte 5 weeks	entering Na mainly at the same crystallographic positions C1,C2,C3 previously occupied by Ca.

4. Conclusion

This study provides direct, atomic-scale insight into the chemical and structural transformations of fibrous zeolites (offretite, mordenite and erionite-Ca) interacting with simulated lung fluid (SLF). Using SC-XRD and SEM, the cation exchange mechanisms and framework modifications were monitored in real time on the same individual crystals, effectively eliminating the influence of impurities and phase heterogeneity that have limited previous investigations. For the carcinogenic erionite, it has been recently hypothesized that cation exchange in the lung environment may play a crucial role in developing lung diseases. In contrast, background knowledge on other fibrous zeolites is limited, and the present study represents a first step toward filling this gap, supported by the comparison of the well-studied erionite case.

Significant Ca-to-Na exchange was observed in all tested zeolites, with erionite exhibiting the fastest kinetics. Offretite and mordenite showed slower but still substantial exchange, and for the first time, structural modifications of fully exchanged offretite were directly observed, potentially having significant relevance to the field of material sciences and related applications. The refined chemical composition of offretite indicated complex charge compensation mechanisms, highlighting the intricate nature of cation substitution in these materials.

These findings advance the understanding of how interfacial processes, including ion migration, protonation, and cation substitution, modify surface chemistry, acidity, and reactivity in fibrous zeolites, with potential implications for their bioreactivity and toxicity. The continuous monitoring of individual single crystals throughout the interaction represents a methodological novelty, providing reliable, time-resolved data.

Overall, this work establishes a robust foundation for future studies investigating more complex systems, including sequential interactions with simulated extracellular and intracellular lung fluids, and contributes to the broader understanding of zeolite behavior at mineral–biological interfaces.

Environmental implication

Erionite is a fibrous zeolite classified as a Group 1 human carcinogen by the International Agency for Research on Cancer. While many aspects of its toxicity mechanisms remain unclear, other fibrous zeolites are under investigation. This study examined the chemical and structural changes of erionite, offretite, and mordenite in contact with simulated lung fluid. For the first time, single crystal X-ray diffraction was used to monitor these changes, eliminating the influence of accessory phases and impurities. A key innovation was the continuous observation of the same single crystal throughout the experiment, providing new insights into ion exchange and structural evolution.

Funding

The author MG is grateful for the Outgoing Visiting Researcher Scholarship 2023 from the University of Urbino Carlo Bo. The authors GC and MG gratefully acknowledge support from the Swiss National Science Foundation through a Scientific Exchange Grant (Grant No. IZSEZ0_230466). This work was also funded by the project INAIL-BRIC ID n. 71/2022 – 001160 to MG and MM (responsible), and the project "Mineralogical, structural and physical-chemical characterization of asbestiform fibrous zeolites" to MG and MM (responsible), in the framework of the 2023 research programs of the Department of Pure and Applied Sciences of the University of Urbino Carlo Bo.

CRediT authorship contribution statement

Matteo Giordani: Writing – review & editing, Writing – original draft, Supervision, Project administration, Investigation, Formal analysis, Data curation, Conceptualization. **Michele Mattioli:** Writing – review & editing. **Georgia Cametti:** Writing – review & editing, Writing – original draft, Supervision, Investigation, Formal analysis, Data curation, Conceptualization.

Declaration of competing interest

The authors declare that they have no known competing financial interests or personal relationships that could have appeared to influence the work reported in this paper.

Acknowledgement

The authors thank Prof. Alfons Berger and Prof. Pierre Lanari for their kind support for SEM-EDX and EMPA measurements. Stephan Brechbühl, Nadine Lötscher and Thomas Aebi are acknowledged for their help in EMPA sample preparation, and Priska Bähler for her support in the wet chemistry lab.

Data availability

Data will be made available on request.

Supplementary materials

Supplementary material associated with this article can be found, in the online version, at doi:10.1016/j.surfin.2026.109054.

References

[1] P. Misaelides, Application of natural zeolites in environmental remediation: a short review, Microporous Mesoporous Mater 144 (2011) 15–18, https://doi.org/10.1016/j.micromeso.2011.03.024.
[2] D.W. Ming, E.R. Allen, Use of natural zeolites in agronomy, horticulture and environmental soil remediation, in: D.L. Bish, D.W. Ming (Eds.), Natural Zeolites: Occurrence, Properties, Applications, Reviews in Mineralogy and Geochemistry, Natural Zeolites: Occurrence, Properties, Applications, Reviews in Mineralogy and Geochemistry, 45, Mineralogical Society of America, Washington, DC, USA, 2001, pp. 619–654, https://doi.org/10.2138/rmg.2001.45.1.
[3] International Agency for Research on Cancer, IARC Working Group on the Evaluation of Carcinogenic Risks to Humans, 1997 silica. Some silicates. Coal Dust and Para-Aramid Fibrils. http://monographs.iarc.fr/ENG/Monographs/vol68/mono68.pdf.
[4] M. Carbone, Y.I. Baris, P. Bertino, B. Brass, S. Comertpay, A.U. Dogan, G. Gaudino, S. Jube, S. Kanodia, C.R. Partridge, H.I. Pass, Z.S. Rivera, I. Steele, M.

UNCORRECTED PROOF

Tuncer, S. Way, H. Yang, A. Miller, Erionite exposure in North Dakota and Turkish villages with mesothelioma, Proc. Natl. Acad. Sci. U.S.A. 108 (33) (2011) 13618–13623, https://doi.org/10.1073/pnas.1105887108.
[5] B. Saini-Eidukat, J.W. Triplet, Erionite and offretite from the Killdeer Mountains, Dunn County, North Dakota, USA, Am. Mineral. 99 (2014) 8–15, https://doi.org/10.2138/am.2014.4567.
[6] M.A. Ortega-Guerrero, G. Carrasco-Núñez, Environmental occurrence, origin, physical and geochemical properties, and carcinogenic potential of erionite near San Miguel de Allende, Mexico, Environ. Geochem. Health 36 (2014) 517–529, https://doi.org/10.1007/s10653-013-9578-z.
[7] E.B. Ilgren, H. Kazemian, J.A. Hoskins, Kandovan the next 'Capadoccia'? A potential public health issue for erionite related mesothelioma risk, Epidemiol. Biostat. Public Health 12 (2015) 1–12, https://doi.org/10.2427/10106.
[8] M. Giordani, M. Mattioli, P. Ballirano, A. Pacella, M. Cenni, M. Boscardin, L. Valentini, Geological occurrence, mineralogical characterization and risk assessment of potentially carcinogenic erionite in Italy, J. Toxicol. Environ. Health B 20 (2017) 81–103, https://doi.org/10.1080/10937404.2016.1263586.
[9] J.P. Patel, M.S. Brook, Erionite asbestiform fibres and health risk in Aotearoa/New Zealand: 1092 A research note, N. Z. Geog. 77 (2021) 123–129, https://doi.org/10.1111/nzg.12291.
[10] D. Di Giuseppe, Characterization of fibrous mordenite: a first step for the evaluation of its potential toxicity, Crystals 10 (2020) 10769, https://doi.org/10.3390/cryst10090769.
[11] M. Giordani, P. Ballirano, A. Pacella, M.A. Meli, C. Roselli, F. Di Lorenzo, I. Fagiolino, M. Mattioli, Another potentially hazardous zeolite from Northern Italy: fibrous mordenite, Minerals 12 (5) (2022) 627 https://doi.org/10.3390/min12050627, a.
[12] M. Mattioli, M. Giordani, P. Arcangeli, L. Valentini, M. Boscardin, A. Pacella, P. Ballirano, Prismatic to asbestiform offretite from Northern Italy: occurrence. Morphology and crystal-chemistry of a new potentially hazardous zeolite, Minerals 8 (2) (2018) 69, https://doi.org/10.3390/min8020069.
[13] M. Mattioli, P. Ballirano, A. Pacella, M. Cangiotti, F. Di Lorenzo, L. Valentini, M.A. Meli, C. Roselli, I. Fagiolino, M. Giordani, Fibrous ferrierite from Northern Italy: mineralogical characterization, surface properties, and assessment of potential toxicity, Minerals 12 (5) (2022) 626, https://doi.org/10.3390/min12050626.
[14] Y. Suzuki, Carcinogenic and fibrogenic effects of zeolites: preliminary observations, Environ. Res. 27 (1982) 433–445, https://doi.org/10.1016/0013-9351(82)90098-6.
[15] Y. Suzuki, N. Kohyama, Malignant mesothelioma induced by asbestos and zeolite in the mouse peritoneal cavity, Environ. Res. 35 (1984) 277–292, https://doi.org/10.1016/0013-9351(84)90136-1.
[16] Y. Suzuki, N. Kohyama, Carcinogenic and fibrogenic effects of erionite, mordenite, and synthetic zeolite 4A, in: D. Kallo, H.S. Sherry (Eds.), Occurrence, Properties and Utilization of Natural Zeolites, Akadémiai Kiadò, Budapest, Hungary, 1988, pp. 829–840.
[17] E. Tátrai, E. Bácsy, J. Kárpáti, G. Ungváry, On the examination of the pulmonary toxicity of mordenite in rats, Pol. J. Occup. Med. Environ. Health 5 (1992) 237–243.
[18] Z. Adamis, E. Tátrai, K. Honma, É. Six, G. Ungváry, In vitro and in vivo tests for determination of the pathogenicity of quartz, diatomaceous earth, mordenite and clinoptilolite, Ann. Occup. Hyg. 44 (2000) 67–74, https://doi.org/10.1093/annhyg/44.1.67.
[19] E. Fach, R. Kristovich, J.F. Long, W.J. Waldman, P.K. Dutta, M.V. Williams, The effect of iron on the biological activities of erionite and mordenite, Environ. Int. 29 (2003) 451–458, https://doi.org/10.1016/S0160-4120(02)00193-9.
[20] D.J. Stephenson, C.I. Fairchild, R.M. Buchan, M.E. Dakins, A fiber characterization of the natural zeolite, mordenite: a potential inhalation health hazard, Aerosol. Sci. Technol. 30 (1990) 467–476, https://doi.org/10.1080/027868299304507.
[21] A.E. Aust, P.M. Cook, R.D. Dodson, Morphological and chemical mechanisms of elongated mineral particle toxicities, J. Toxicol. Environ. Health B 14 (2001) 40–75, https://doi.org/10.1080/10937404.2011.556046.
[22] World Health Organization (WHO), Asbestos and Other Natural Mineral Fibers, 53, Environmental Health Criteria, Geneva, Switzerland, 1986, pp. 69–107.
[23] National Institute for Occupational Safety and Health (NIOSH), NIOSH method 7400, asbestos and other fibers by PCM. NIOSH Manual of Analytical Methods, 4th ed., 1994 a.
[24] P. Bertino, A. Marconi, L. Palumbo, B.M. Bruni, D. Barbone, S. Germano, A.U. Dogan, G.F. Tassi, C. Porta, L. Mutti, et al., Erionite and asbestos differently cause transformation of human mesothelial cells, Int. J. Cancer 121 (2007) 2766–2774, https://doi.org/10.1002/ijc.22687.
[25] L.V.M. De Assis, M.C. Isoldi, The function, mechanisms, and role of the genes PTEN and TP53 and the effects of asbestos in the development of malignant mesothelioma: a review focused on the genes' molecular mechanisms, Tumor Biol. 35 (2014) 889–901, https://doi.org/10.1007/s13277-013-1210-4.
[26] A.F. Gualtieri, Towards a quantitative model to predict the toxicity/pathogenicity potential of mineral fibers, Toxicol. Appl. Pharmacol. 361 (2018) 89–98, https://doi.org/10.1016/j.taap.2018.05.012.
[27] M. Betti, M.G. Nasoni, F. Luchetti, M. Giordani, M. Mattioli, Potential toxicity of natural fibrous zeolites: in vitro study using Jurkat and HT22 cell lines, Minerals 12 (8) (2022) 988, https://doi.org/10.3390/min12080988.
[28] D. Di Giuseppe, S. Scarfì, A. Alessandrini, A.M. Bassi, S. Mirata, V. Almonti, G. Ragazzini, A. Mescola, M. Filaferro, R. Avallone, G. Vitale, Acute cytotoxicity of mineral fibres observed by time-lapse video microscopy, Toxicology 466 (2022) 153081, https://doi.org/10.1016/j.tox.2021.153081.
[29] H.F. Lodish, A. Berk, P. Matsudaira, C.A. Kaiser, M. Krieger, M.P. Scott, L. Zipursky, J. Darnell, Molecular Cell Biology, MacMillan, 1999, p. 1184.
[30] E. Innes, H.H.P. Yiu, P. McLean, W. Brown, M. Boyles, Crit. Rev. Toxicol. 51 (2021) 217–248.
[31] P. Ballirano, G. Cametti, Crystal chemical and structural modifications of erionite fibers leached with simulated lung fluids, Am. Mineral. 100 (4) (2015) 1003–1012, https://doi.org/10.2138/am-2015-4922.
[32] M. Giordani, G. Cametti, F. Di Lorenzo, S.V. Churakov, Real-time observation of fibrous zeolites reactivity in contact with simulated lung fluids (SLFs) obtained by atomic force microscope (AFM), Minerals 9 (2) (2019) 83, https://doi.org/10.3390/min9020083.
[33] A. Pacella, P. Ballirano, M. Fantauzzi, A. Rossi, C. Viti, L. Arrizza, E. Nardi, R. Caprioli, M.R. Montereali, Surface and bulk modifications of fibrous erionite in mimicked Gamble's solution at acidic pH, Minerals 11 (9) (2021) 914, https://doi.org/10.3390/min11090914.
[34] M.C. Di Carlo, P. Ballirano, M.R. Montereali, R. Caprioli, E. Nardi, A. Pacella, An insight on possible toxicity mechanism of fibrous erionite, Period. Mineral. 92 (2) (2023) 191–201, https://doi.org/10.13133/2239-1002/18097.
[35] S. Raneri, A. Gianoncelli, V. Bonanni, S. Mirata, S. Scarfì, L. Fornasini, D. Bersani, D. Baroni, C. Picco, A.F. Gualtieri, The influence of cation exchange on the possible mechanism of erionite toxicity: a synchrotron-based micro-X-ray fluorescence study on THP-1-derived macrophages exposed to erionite-Na, Environ. Res. 252 (2024) 118878, https://doi.org/10.1016/j.envres.2024.118878.
[36] C.M. Bergamini, S. Gambetti, A. Dondi, C. Cervellati, Oxygen, reactive oxygen species and tissue damage, Curr. Pharm. Des. 10 (14) (2004) 1611–1626, https://doi.org/10.2174/1381612043384664.
[37] M. Tam, S. Gomez, M. Gonzalez-Gross, A. Marcos, Possible roles of magnesium on the immune system, Eur. J. Clin. Nutr. 57 (10) (2003) 1193–1197, https://doi.org/10.1038/sj.ejcn.1601689.
[38] A.F. Gualtieri, Journey to the centre of the lung. The perspective of a mineralogist on the carcinogenic effects of mineral fibres in the lungs, J. Hazard. Mater. 442 (2023) 130077, https://doi.org/10.1016/j.jhazmat.2022.130077.
[39] A. Bononi, C. Giorgi, S. Patergnani D. Larson, K. Verbruggen, M. Tanji, L. Pellegrini, V. Signorato, F. Olivetto, S. Pastorino, M. Nasu, A. Napolitano, G. Gaudino, P. Morris, G. Sakamoto, L.K. Ferris, A. Danese, A. Raimondi, C. Tacchetti, S. Kuchay, H.I. Pass, E.B. Affar, H. Yang, P. Pinton, M. Carbone, BAP1 regulates IP3R3-mediated Ca2+ flux to mitochondria suppressing cell transformation, Nature 546 (2017) 549–553, https://doi.org/10.1038/nature22798.
[40] P. Ballirano, A. Pacella, S. Mirata, M. Passalacqua, M.C. Di Carlo, L. Arrizza, M.R. Montereali, S. Scarfì, Fibrous erionite modifications following THP-1 macrophage phagocytosis: an insight into the mechanisms of interaction with biological systems, J. Hazard. Mater. 489 (2025) 137546, https://doi.org/10.1016/j.jhazmat.2025.137546.
[41] A. Pacella, M. Fantauzzi, D. Atzei, C. Cremisini, E. Nardi, M.R. Montereali, A. Rossi, P. Ballirano, Iron within the erionite cavity and its potential role in inducing its toxicity: evidence of Fe (III) segregation as extra-framework cation, Microporous Mesoporous Mater. 237 (2017) 168–179, https://doi.org/10.1016/j.micromeso.2016.09.021.
[42] M. Dogan, Quantitative characterization of the mesothelioma-inducing erionite series minerals by transmission electron microscopy and energy dispersive spectroscopy, Scanning 34 (1) (2012) 37–42, https://doi.org/10.1002/sca.20276.
[43] C. Giacobbe, A. Moliterni, D. Di Giuseppe, D. Malferrari, J.P. Wright, M. Mattioli, S. Raneri, C. Giannini, L. Fornasini, E. Mugnaioli, P. Ballirano, The crystal structure of the killer fibre erionite from Tuzköy (Cappadocia, Turkey), IUCrJ. 10 (4) (2023) 397–410, https://doi.org/10.1107/S2052252523003500.
[44] M. Giordani, M.G. Nasoni, E. Bargagni, M. Cangiotti, F. Luchetti, M. Mattioli, Fibrous zeolites and pulmonary fibroblasts: toxicological impact and EPR-based insights into cellular alterations. Unpublished results.
[45] M. Rozalen, M.E. Ramos, F.J. Huertas, S. Fiore, F. Gervilla, Dissolution kinetics and biodurability of tremolite particles in mimicked lung fluids: effect of citrate and oxalate, J. Asian Earth Sci. 77 (2013) 318–326, https://doi.org/10.1016/j.jseaes.2013.04.008.
[46] J.I. Goldstein, D.E. Newbury, P. Echlin, D.C. Joy, A.D. Roming, C.E. Lyman, C. Fiori, E. Lifshin, Scanning Electron Microscopy and X-Ray Microanalysis, 2nd ed., Plenum Press, New York, NY, 1992.
[47] A. Pacella, P. Ballirano, G. Cametti, Quantitative chemical analysis of erionite fibres using a micro-analytical SEM-EDX method, Eur. J. Mineral. 28 (2016) 257–264, https://doi.org/10.1127/ejm/2015/0027-2497.
[48] E. Passaglia, The crystal chemistry of chabazites, Am. Mineral. 55 (1970) 1278–1301.
[49] G. Cametti, A. Pacella, F. Mura, M. Rossi, P. Ballirano, New morphological, chemical, and structural data of woolly erionite-Na from Durkee, Oregon, USA, Am. Mineral. 98 (2013) 2155–2163.
[50] A.U. Dogan, M. Dogan, *Re*-evaluation and re-classification of erionite series minerals, Environ. Geochem. Health 30 (2008) 355–366.
[51] L.S. Campbell, J. Charnock, A. Dyer, S. Hillier, S. Chenery, F. Stoppa, C.M.B. Henderson, R. Walcott, M. Rumsey, Determination of zeolite-group mineral compositions by electron probe microanalysis, Mineral. Mag. 80 (5) (2016) 781–807, https://doi.org/10.1180/minmag.2016.080.044.
[52] CrysAlisPro 1.171.43.144a [software], Rigaku Oxford Diffraction, 1995-2024.
[53] G.M. Sheldrick, SHELXT- integrated space group and crystal structure determination [software], Acta Crystallogr. A: Found. Adv. 71 (2014) 3–8.
[54] G.M. Sheldrick, Crystal structure refinement with SHELXL [software], Acta Crystallogr. C 71 (2015) 3–8.
[55] L.J. Farrugia, WingX suite for small-molecule single-crystal crystallography [software], J. Appl. Cryst. 32 (1999) 837–838.

UNCORRECTED PROOF

[56] J.A. Gard, J.M. Tait, The crystal structure of the zeolite offretite, K1. 1Ca1. 1Mg0. 7 [Si12. 8Al5. 2O36]. 15.2 H2O, Struct. Sci. 28 (3) (1972) 825–834, https://doi.org/10.1107/S0567740872003279.
[57] A. Alberti, P. Davoli, G. Vezzalini, The crystal structure refinement of a natural mordenite, Z. Krist.-Cryst. Mater. 175 (1–4) (1986) 249–256.
[58] A. Alberti, A. Martucci, E. Galli, G. Vezzalini, A reexamination of the crystal structure of erionite, Zeolites 19 (5–6) (1997) 349–352, https://doi.org/10.1016/S0144-2449(97)00102-4.
[59] K. Momma, F. Izumi, VESTA 3 for three-dimensional visualization of crystal, volumetric and morphology data [software], J. Appl. Crystallogr. 44 (2011) 1272–1276.
[60] J.L. Schlenker, J.J. Pluth, J.V. Smith, Positions of cations and molecules in zeolites with the mordenite-type framework: VIII dehydrated sodium-exchanged mordenite, Mater. Res. Bull. 14 (6) (1979) 751–758, https://doi.org/10.1016/0025-5408(79)90134-X.
[61] R.M. Barrer, I.M. Galabova, Ion-exchanged forms of Zeolite L, Erionite, and offretite and sorption of inert gases, (1973) 356–373. Doi: 10.1021/ba-1973-0121.ch032.
[62] F. Turci, M. Tomatis, A. Pacella, Surface and bulk properties of mineral fibres relevant to toxicity, in: A.F. Gualtieri (Ed.), Mineral Fibres: Crystal Chemistry, Chemical-Physical Properties, Biological Interaction and Toxicity, Mineral Fibres: Crystal Chemistry, Chemical-Physical Properties, Biological Interaction and Toxicity, 18, European Mineralogical Union Notes in Mineralogy, 2017, https://doi.org/10.1180/EMU-notes.18.
[63] M. Carbone, S. Emri, A.U. Dogan, I. Steele, M. Tuncer, H.I. Pass, Y.I. Baris, A mesothelioma epidemic in Cappadocia: scientific developments and unexpected social outcomes, Nat. Rev. Cancer 7 (2) (2007) 147–154, https://doi.org/10.1038/nrc2068.
[64] IARC International Agency for Research on Cancer, Arsenic, metals, fibres, and dusts, IARC Monogr. Eval. Carcinog. Risks. Hum. 100C (2012) VolLyon.
[65] E. Gazzano, E. Foresti, I.G. Lesci, M. Tomatis, C. Riganti, B. Fubini, N. Roveri, D. Ghigo, Different cellular responses evoked by natural and stoichiometric synthetic chrysotile asbestos, Toxicol. Appl. Pharmacol. 206 (3) (2005) 356–364, https://doi.org/10.1016/j.taap.2004.11.021.
[66] P. Ballirano, A. Pacella, C. Cremisini, E. Nardi, M. Fantauzzi, D. Atzei, A. Rossi, G. Cametti, Fe (II) segregation at a specific crystallographic site of fibrous erionite: a first step toward the understanding of the mechanisms inducing its carcinogenicity, Microporous Mesoporous Mater. 211 (2015) 49–63, https://doi.org/10.1016/j.micromeso.2015.02.046.
[67] M. Giordani, S. Mirata, S. Scarfi, M. Passalacqua, L. Fornasini, G. Drava, M.A. Meli, C. Roselli, M. Mattioli, The cytotoxic/genotoxic role of impurities in soluble minerals: the case of natural (fibrous epsomite) versus synthetic (Epsom salt) magnesium sulphate, Sci. Total Environ. 966 (2025) 178666, https://doi.org/10.1016/j.scitotenv.2025.178666.

UNCORRECTED PROOF